

## Article

# Optimization of Sweep and Blade Lean for Diffuser to Suppress Hub Corner Vortex in Multistage Pump

Chao Ning<sup>1</sup>, Puyu Cao<sup>1,\*</sup>, Xuran Gong<sup>1</sup> and Rui Zhu<sup>2</sup>

<sup>1</sup> National Research Center of Pumps, Jiangsu University, Zhenjiang 212013, China; 2111811011@stmail.ujs.edu.cn (C.N.); 2221811011@stmail.ujs.edu.cn (X.G.)

<sup>2</sup> Department of Fluid Machinery and Engineering, Xi'an Jiaotong University, Xi'an 710049, China; ruizhu@stu.xjtu.cn

\* Correspondence: mafatu1988@ujs.edu.cn

**Abstract:** The bowl diffuser is the main flow component in multistage submersible pumps; however, secondary flow fields can easily induce a separation vortex in the hub corner region of the bowl diffuser during normal operation. To explore the flow mechanism of the hub corner separation vortex and develop a method for suppressing hub corner separation vortices, the lean and sweep of the diffuser blade were optimized using computational fluid dynamics (CFD) simulations and central composite design. Diffuser efficiency, static pressure recovery coefficient, and non-uniformity were selected as the optimization objectives. Details of the internal flow were revealed and the collaborative response relationships between blade lean/sweep parameter equations and optimization objectives were established. The optimization results show that a greater pressure difference between the pressure surface and suction surface (PS–SS) at the inlet can offset transverse secondary flow, whereas a lower PS–SS pressure difference will cause a drop in low-energy fluid in the diffuser mid-section. The blade's lean scheme suppresses the hub corner separation vortex, leading to an increase in pressure recovery and diffuser efficiency. Moreover, optimizing the sweep scheme can reduce the shroud–hub pressure difference at the inlet to offset spanwise secondary flow and enhance the hub–shroud pressure difference at the outlet, thus driving low-energy fluid further downstream. The sweep scheme suppresses the hub corner vortex, with a resulting drop in non-uniformity of 13.1%. Therefore, optimization of the diffuser blade's lean and sweep can result in less low-energy fluid or drive it further away from hub, thereby suppressing the hub corner vortex and improving hydraulic performance. The outcomes of this work are relevant to the advanced design of bowl diffusers for multistage submersible pumps.

**Keywords:** multistage submersible pump; bowl diffuser; parametric design; secondary flow



**Citation:** Ning, C.; Cao, P.; Gong, X.; Zhu, R. Optimization of Sweep and Blade Lean for Diffuser to Suppress Hub Corner Vortex in Multistage Pump. *Machines* **2021**, *9*, 316. <https://doi.org/10.3390/machines9120316>

Academic Editor: Davide Astolfi

Received: 27 October 2021

Accepted: 25 November 2021

Published: 26 November 2021

**Publisher's Note:** MDPI stays neutral with regard to jurisdictional claims in published maps and institutional affiliations.



**Copyright:** © 2021 by the authors. Licensee MDPI, Basel, Switzerland. This article is an open access article distributed under the terms and conditions of the Creative Commons Attribution (CC BY) license (<https://creativecommons.org/licenses/by/4.0/>).

## 1. Introduction

The multi-stage submersible pump is widely used in various fields, mainly owing to its strong adaptability and easy pressurization [1]. However, complex and changeable working conditions present strict requirements for operational stability. The impeller and bowl diffuser are the main components in each stage of the pump. The head can be adjusted by changing the stage of the pump to meet the requirements of different applications. However, multi-stage submersible pumps with a bowl diffuser typically suffer from low efficiency and high operating costs. The bowl diffuser flow channel is curved and the fluid has a large impact on the inlet. Moreover, pump losses are dominated by the separation vortex in the hub corner of the diffuser. Therefore, optimization of the bowl diffuser is crucial to improving the single-stage head and overall working performance of the multistage submersible pump.

To date, numerous studies on the optimization of impellers and diffusers in pumps have been published [2,3]. To determine the algebraic relationship between the structural

parameters of pumps and optimization objectives, data can be more efficiently and accurately analyzed using computational fluid dynamics (CFD) [4–6]. To obtain the optimal solution, CFD simulations are often combined with optimization design methods, such as the response surface method, neural network simulations, and orthogonal experiments [7–9]. Tong et al. [10] used numerical simulations and the Latin hypercube sampling method to construct functional relationships among independent variables and optimization objectives. Then, the second-generation genetic algorithm was used to solve the multi-objective optimization problem for a centrifugal pump. Stel et al. [11] studied the influence of pump stage on the performance of a multi-stage submersible pump using a CFD method based on the finite volume approach and investigated the transient flow characteristics in the pump under different flow rates. Heo et al. [12] compared three approximate models based on the response surface function (RSF), Kriging response surface, and a neural network for finding Pareto-optimal solutions which are set in the independent variable domain of the centrifugal pump.

The approximate model design method has been widely used in pump design [13,14]. Previous approaches could be applied to the optimization of other structural parameters, such as blade inlet and outlet angle, blade number, and blade thickness. Nonetheless, optimization techniques to achieve an optimal diffuser design that maximizes performance and stability of the overall stage are still lacking. Recently, design optimization strategies have been widely applied in the field of pneumatic fluid machinery, including the design of blade lean and sweep. A brief review is presented herein.

Rosic et al. [15] analyzed the influence of the stationary blade stacking combination on turbine performance. Razavi et al. [16] designed transonic rotor blades with different degrees of sweep and tilt. The blades were optimized using a neural network-based multi-objective optimization method, with efficiency, operating range, and stage pressure ratio as the target variables. He et al. [17,18] studied the influence of blade sweep design on transonic impeller performance through numerical simulations. The results showed that a forward-swept shroud design reduces the forward load, impact strength, and leakage vortex. A back-swept hub design suppresses the blade front load and the separation of secondary flow, thereby reducing losses near the hub. Bagshaw et al. [19] designed specially shaped cascade end walls with reverse load tilting, which can effectively inhibit the development of secondary flow in cascades. Goto et al. [20,21] used the color oil film flow display technology to capture large-scale separation vortices in the suction surface corner region of the diffuser and showed that the flow separation vortex is a source of hydraulic losses in the diffuser. Scillito et al. [22] used the large-eddy simulation method to confirm that axial compressor losses are dominated by the three-dimensional flow region near the diffuser end wall, two-dimensional laminar flow separation, and the diffuser outlet wake. The influence of inlet turbulence on sources of loss was further investigated.

In summary, blade lean and sweep design are widely used in compressor and turbine blades [23,24]; however, these approaches are rarely applied to water pumps, in particular, the bowl diffuser. The present study aimed to address these limitations by applying the design ideas and methods used for pneumatic machinery to the bowl diffuser of a multistage submersible pump. This research provides a scientific basis for follow-up research on diffuser design optimization.

The remainder of this paper is organized as follows. Section 2 describes the numerical model and simulation setup. Details of the experimental detection method are presented in Section 3. In Section 4, optimized designs of the blade lean and sweep of the bowl diffuser are presented based on the concept of parametric equations. In Section 5, the influence of various design schemes on the hydraulic characteristics of the diffuser are discussed and the collaborative response relationship between the parameter equation and the hydrodynamic performance of the diffuser is established. Section 6 discusses the effect of various optimization strategies on the hub corner separation vortex in the diffuser. Finally, the main conclusions of this work are summarized in Section 7.

## 2. Numerical Model and Simulation Setup

### 2.1. Computational Domain

In this paper, a Q80-20 multi-stage submersible pump with a bowl diffuser was selected as the research object. The basic parameters of the main flow passage parts of the multi-stage submersible pump are as follows: design flow rate,  $Q = 80 \text{ m}^3 \cdot \text{h}^{-1}$ ; single-stage head,  $H = 18 \text{ m}$ ; rotating speed,  $n = 2850 \text{ r/min}$ . The main structural parameters of the impeller and the bowl diffuser are presented in Tables 1 and 2. Geometric models of the impeller and bowl diffuser of the multistage submersible pump are shown in Figure 1.

**Table 1.** The main structural parameters of the impeller.

Parameters	Value
Blade number of impeller $Z$	7
Diameter of inlet $d_1$ (mm)	97
Diameter of outlet $d_2$ (mm)	134
Width of blade outlet $b_2$ (mm)	20
Inlet angle of hub $\beta_1$ ( $^\circ$ )	28
Outlet angle of hub $\beta_2$ ( $^\circ$ )	34.2

**Table 2.** The main structural parameters of the bowl diffuser.

Parameters	Value
Blade number of diffuser $Z_d$	8
Diameter of outlet $d_4$ (mm)	95
Axial length $e$ (mm)	152
Inlet angle of hub $\beta_3$ ( $^\circ$ )	13.7
Outlet angle of hub $\beta_4$ ( $^\circ$ )	90
Wrap angle of hub $\phi_{\text{Hub}}$ ( $^\circ$ )	83
Wrap angle of shroud $\phi_{\text{Shroud}}$ ( $^\circ$ )	60

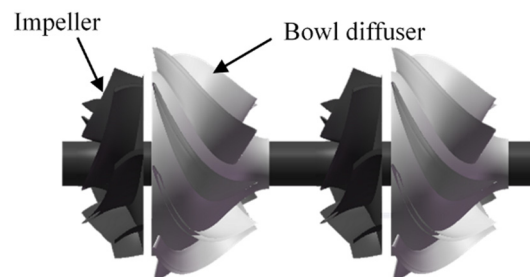
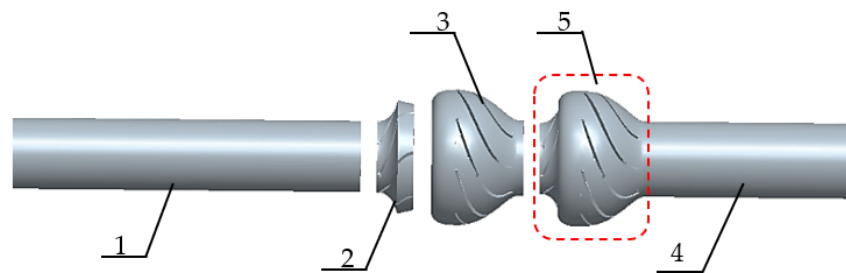


**Figure 1.** Geometrical model of the impeller and bowl diffuser.

According to Shi et al. [25], the internal flow characteristics in the second stage of the pump are basically the same as those in the later stages. Therefore, the following tests were based on data obtained from the second stage of the pump. To consider all stages, a large number of grid elements must be generated, which dramatically increases the calculation time. To balance computation time and numerical accuracy, Zhou et al. [26] demonstrated that two stages can be used to represent the whole pump system; therefore, the two-stage pump model was selected for the present work. The three-dimensional (3D) pump modeling software CFTurbo was used to model the whole flow field of the pump, as shown in Figure 2. The calculation domain is mainly comprised of the inlet pipe, impeller, bowl diffuser, and outlet pipe. Each stage of the impeller and bowl diffuser constitutes a pressurization unit, and there are two pressurization units in total. To ensure fully developed fluid flow and improve the flow field calculation accuracy, the inlet pipe, outlet pipe, and outlet of the bowl diffuser were extended appropriately.



1.inlet pipe 2. impeller water 3. bowl diffuser water 4. outlet pipe 5. pressurization

**Figure 2.** Multistage submersible pump calculation domain.

### 2.2. Mesh Generation

The ANSYS ICEM CFD software package was used to generate an unstructured mesh as the calculation domain. Key regions of the mesh were locally refined. Six grids of various sizes were selected to verify the grid independence of the calculation domain and ensure a grid quality greater than 0.3. As seen in Table 3, the simulation results become stable as the total number of grid elements increases. When the total number of elements is 6.8 million or higher, further changes in the calculated head and efficiency are very small, suggesting that the number of grid elements no longer has an effect on the calculation results. To balance computation time and solution accuracy, the total number of grid elements was selected as approximately 6.8 million. The generated mesh is shown in Figure 3.

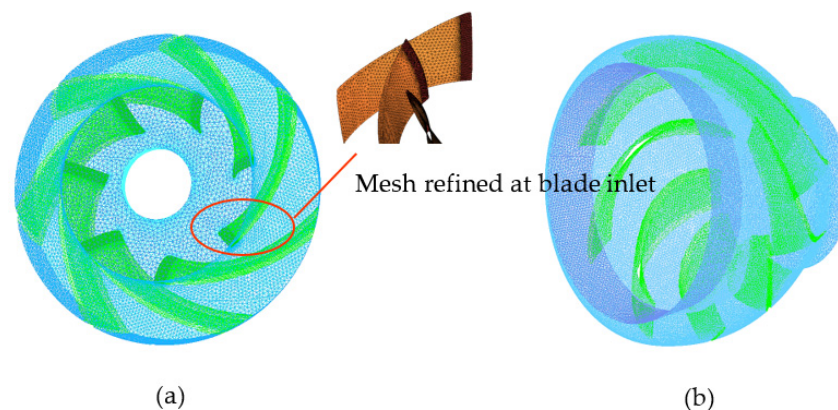


**Figure 3.** Mesh of impeller and diffuser for multistage submersible pump. (a) Mesh of impeller. (b) Mesh of diffuser.

**Table 3.** Influence of the grid number on accuracy.

Parameter	$N (\times 10^4 \times 10^4)$	H/m	$\eta/\%$
value	302	33.20	95.04
	410	33.04	95.00
	553	32.86	94.91
	680	32.74	94.88
	837	32.69	94.88
	988	32.70	94.88

### 2.3. Turbulent Model

The standard  $k-\epsilon$  model is based on turbulent kinetic energy ( $k$ ) transport and turbulent energy dissipation rate ( $\epsilon$ ) transport and offers good robustness and economy in predicting the flow characteristics of most flow fields reasonably and accurately. However, the standard  $k-\epsilon$  model is prone to errors when calculating flow over a complex curved wall [27].

To account for the high-speed rotation domain and large variation in curvature of the wall in the calculation domain of the multi-stage submersible pump, the RNG  $k$ - $\varepsilon$  model proposed by Yakhot et al. [28] was selected, which is suitable for flows with separation [29]. Compared with the standard  $k$ - $\varepsilon$  model, the RNG  $k$ - $\varepsilon$  model contains an additional time average strain rate ( $E_{ij}$ ) in the reaction mainstream equation of  $\varepsilon$ , which can improve the accuracy for swirl flow and more reasonably deal with flow near the wall [30,31]. The two transport equations can be expressed, as follows:

The turbulent kinetic energy  $k$  transport equation:

$$\frac{\partial(\rho k u_i)}{\partial x_i} + \frac{\partial(\rho k)}{\partial t} = \frac{\partial}{\partial x_j} \left[ \left( \mu + \frac{\mu_t}{\sigma_k} \right) \frac{\partial k}{\partial x_j} \right] + P_k - \rho \quad (1)$$

The turbulent energy dissipation rate  $\varepsilon$  equation is:

$$\frac{\partial(\rho \varepsilon u_i)}{\partial x_i} + \frac{\partial(\rho \varepsilon)}{\partial t} = \frac{\partial}{\partial x_j} \left[ \left( \mu + \frac{\mu_t}{\sigma_\varepsilon} \right) \frac{\partial \varepsilon}{\partial x_j} \right] + \frac{\varepsilon}{k} (c_1^* P_k - c_2 \rho \varepsilon) \quad (2)$$

where  $k$  is turbulent kinetic energy,  $m^2/s^2$ ;  $\varepsilon$  is turbulent energy dissipation rate,  $m^2/s^3$ ;  $P_k$  is the pressure generating term caused by the velocity gradient;  $\mu_t$  is the turbulent viscosity.

#### 2.4. Simulation Setup

ANSYS CFX 17.1 was used to calculate the steady three-dimensional whole flow field of the model pump under the design conditions. The fluid in the pump was set as incompressible water. The RNG  $k$ - $\varepsilon$  model was selected for the simulation calculations to satisfy the solution accuracy requirement. The boundary conditions were set, as follows: the inlet boundary condition was set as pressure inlet and the static pressure as 0 Pa; The outlet boundary condition was set to the mass flow outlet condition. The adiabatic nonslip solid wall boundary condition was adopted at the wall and the near wall area was treated as a scalable wall function.

The steady numerical calculation was carried out across the whole calculation domain of the multistage submersible pump. The impeller part was considered the rotating domain and the bowl diffuser part was considered the static domain. The interfaces between the rotating section and the static section were set as the dynamic and static interfaces, and the frozen rotor model was used to handle them. The General Grid Interface (GGI) was used as the grid connection method for dealing with the static interface. The root mean square (RMS) value for convergence accuracy was set to  $5 \times 10^{-5}$ .

### 3. Experimental Pump Characteristics

To verify the simulation method, the head obtained using CFD was compared with experimental head values in the flow range of 0.8Qd–1.1Qd. The test-bed, shown in Figure 4, is composed of a flow control device, a data acquisition device, and a data processing device [32,33]. The flow rate was adjusted by the valve and measured by the electromagnetic flowmeter.

The comparison of head obtained by experiment and simulation was shown in Figure 5. The average error between the numerical simulation results and the experimental results was less than 5%, and the relative error of the head under the design conditions was 2.7%. Errors between the simulation results and experimental results were within the allowable range. The results indicate that the simulation calculation can accurately predict the performance of the multistage submersible pump under the design conditions.

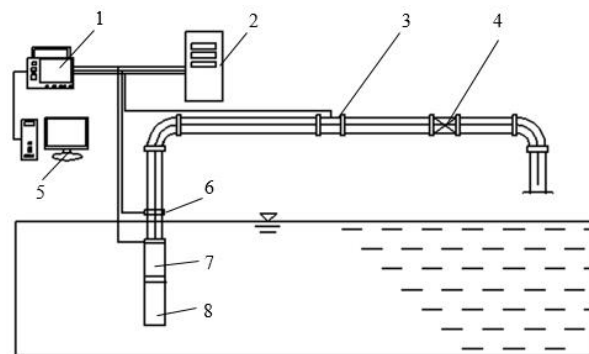


**Figure 4.** Testing apparatus [32]. 1. Data acquisition instrument. 2. Frequency inverter. 3. Electro-magnetic flowmeter. 4. The valve. 5. Computer. 6. Pressure sensor. 7. Pump. 8. Motor.

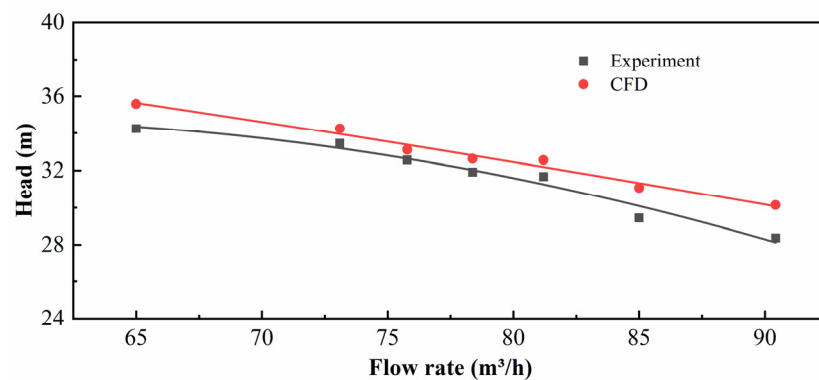


**Figure 5.** Comparison of head obtained by experiment and simulation.

#### 4. Optimization Schemes

##### 4.1. Design of Blade Lean

The coordinate system of the blade inlet profile was established, as shown in Figure 4. The origin of the coordinate system is defined as the intersection between the blade inlet edge and the hub. The positive direction of the ordinate axis is from the hub to the shroud of the diffuser, expressed by the spanwise coefficient  $Sp_1$ . The circumferential direction is the positive direction of the abscissa, represented by  $f(Sp_1)$ . The starting angle of any point at the inlet edge of the blade refers to the angle between the line connecting the point to the center point and the axial plane with a starting angle of zero, indicated by  $\theta$  in Figure 6.

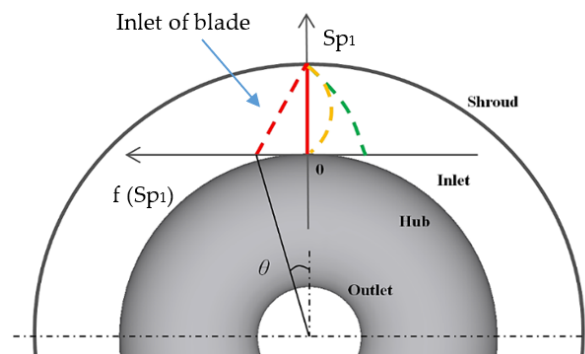


**Figure 6.** Blade lean coordinate system and blade leading edge angle of diffuser (from inlet view).

It is assumed that the parabolic equation governing the blade inlet profile is:

$$f(Sp_1) = a_0 + a_1Sp_1 + a_2Sp_1^2 \tag{3}$$

where spanwise coefficient  $Sp_1 \in [0,1]$ , 0 for the hub and 1 for the shroud;  $a_0$ ,  $a_1$ , and  $a_2$  are the parameters to be optimized. The difference between the starting angle of the hub and the shroud is referred to as the starting angle difference  $\Delta\theta$ , defined as

$$\Delta\theta = \theta_{Hub} - \theta_{Shroud} \quad (4)$$

where  $\theta_{Hub}$  is the starting angle of the hub at the blade inlet,  $\theta_{Hub} = a_0$ ;  $\theta_{Shroud}$  is the starting angle of the shroud at the blade inlet,  $\theta_{Shroud} = a_0 + a_1 + a_2$ ,  $\Delta\theta = a_1 + a_2$ . The factors and the levels used in the central composite designs are presented in Table 4.

**Table 4.** Factors and levels for the central composite design.

Levels	Factors		
	$a_0$	$a_1$	$a_2$
−1.682	−12.07	−17.73	8.93
−1	−9	−15	12
0	−4.5	−11	16.5
1	0	−7	21
1.682	3.07	−4.27	24.06

#### 4.2. Design of Sweep

Figure 5 shows the sweep coordinate system in the meridian plane of the diffuser. The positive direction of the longitudinal axis is defined as the direction from the hub to the shroud, expressed by the spanwise coefficient  $Sp_2$ . The axis is the positive direction of the abscissa, represented by  $f(Sp_2)$ . The origin is the intersection between the hub and the blade outlet edge. It is assumed that the parabolic equation governing the blade inlet profile is

$$f(Sp_2) = b_0 + b_1Sp_2 + b_2Sp_2^2 \quad (5)$$

where  $Sp_2$  is the spanwise coefficient;  $Sp_2 \in [0,1]$ , 0 for hub and 1 for shroud.

As shown in Figure 7,  $b_0$  is located at the edge of the outlet on the hub,  $b_1$  is located at the edge of the outlet on the shroud, and  $b_2$  is located at the edge of the inlet on the hub, selected as the independent factors. The values are presented in Table 5. The sweep angle  $\beta$  is the angle between the new outlet edge of the blade and the original outlet edge of the blade. When the position of the blade outlet edge on the hub remains unchanged and the position of the shroud moves in the positive direction along the abscissa,  $\beta$  is negative; when moving in the negative direction along the abscissa,  $\beta$  is positive. Here, the positive and negative signs indicate direction only.

**Table 5.** Factors and levels for the central composite design.

Levels	Factors		
	$b_0$	$b_1$	$b_2$
−1.682	−3.05	10.61	−55.36
−1	−1	13	−54
0	2	16.5	−52
1	5	20	−50
1.682	7.05	22.39	−48.64

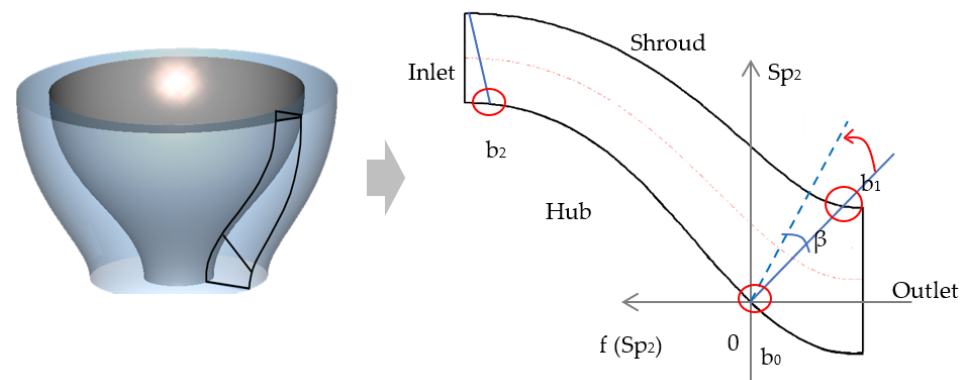


**Figure 7.** Sweep coordinate system and blade sweep angle of diffuser sweep design (from meridional view).

#### 4.3. Analysis Parameters

Diffuser efficiency  $\eta$ , static pressure recovery coefficient  $Cp$ , and non-uniformity  $\zeta_i$  were selected to evaluate the hydrodynamic performance of the diffuser before and after optimization. The diffuser efficiency is  $\eta = P_{t4}/P_{t3}$ .  $P_{t3}$  is the total pressure at the inlet of the diffuser and  $P_{t4}$  is the total pressure at the outlet of the diffuser. Static pressure recovery coefficient is  $Cp = (P_{s4} - P_{s3})/P_{s3}$ ,  $P_{s3}$  is the static pressure at the inlet of the diffuser and  $P_{s4}$  is the static pressure at the outlet of the diffuser.  $Cp$  indicates the potential for converting kinetic energy into static pressure energy as fluid flows through the diffuser. An increase in  $Cp$  indicates enhanced static pressure recovery ability.

The non-uniformity  $\zeta_i$  is an index for quantitatively evaluating flow uniformity at the outlet of the diffuser. The efficiency and operating stability of the pump are inversely affected by flow uniformity in the diffuser and impeller. As flow uniformity increases at the outlet of the diffuser,  $\zeta_i$  decreases; conversely, as the flow becomes less uniform,  $\zeta_i$  increases. The formula for calculating the non-uniformity  $\zeta_i$  is

$$\zeta_i = \frac{1}{Q} \int_{A_i} \sqrt{(V_z - V_{F,av,i})^2} dA \quad (6)$$

where  $Q$  is the design flow rate;  $V_z$  is the local axial velocity in the flow section, m/s. Here, the section is the outlet surface of the diffuser and  $V_{F,av,i}$  is the average velocity at the outlet surface of the diffuser, m/s.

## 5. Results

### 5.1. Response Surface of the Blade Lean Optimized Diffuser

Factor  $a_0$  represents the starting angle of the blade on the hub surface,  $a_1$  is related to the position of the axis, and  $a_2$  affects the opening size of the parabola. The influence of pairs of factors on the response value was analyzed by fixing any one of the three factors  $a_0$ ,  $a_1$ , and  $a_2$  to zero. Figure 8a,b show that the opening of the response surface is downward, and the trend is consistent when  $a_2$  is at a medium level or  $a_1$  is at a medium level. The radian of the curve increases when the starting angle on the hub surface is  $-4.5^\circ$  (medium  $a_0$ ), the symmetrical axis moves to hub (high  $a_1$ ), and the opening of parabola decreases (high  $a_2$ ), which improves the diffuser efficiency. Figure 8c shows that the interaction between factors  $a_1$  and  $a_2$  is significant when  $a_0$  is medium. The interaction between  $a_1$  and  $a_2$  results in optimal diffuser efficiency when both  $a_1$  and  $a_2$  are high.

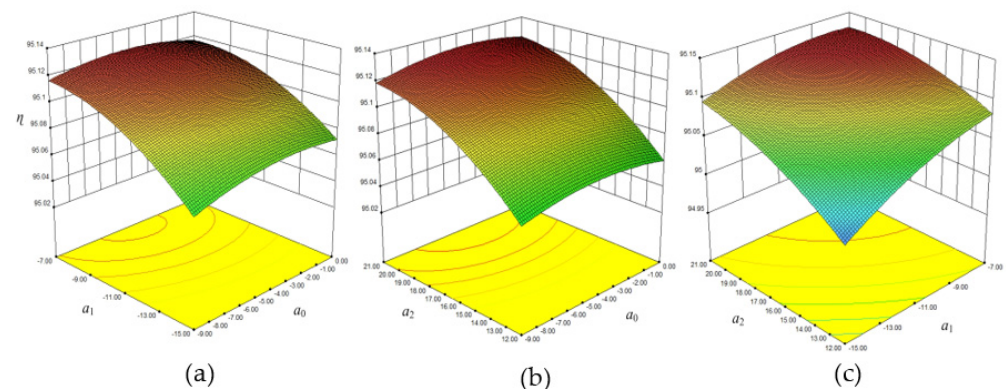


**Figure 8.** Response surface of diffuser efficiency in blade lean optimization (a)  $a_2 = 0$ . (b)  $a_1 = 0$ . (c)  $a_0 = 0$ .

Figure 9a shows that the static pressure recovery coefficient reaches the optimal value when  $a_0$  is above the medium level and  $a_1$  is at the medium level on the low side. A medium–high level of  $a_0$  indicates that the starting angle of the hub at the blade inlet  $\theta \in (0^\circ, 4.5^\circ)$ . A medium–low level of  $a_1$  indicates that the symmetrical axis of the curve deviates from the shroud, therefore, movement of the symmetrical axial can improve the conversion rate of kinetic energy to static pressure in the diffuser. Figure 9b shows that the static pressure recovery coefficient is optimal when  $a_0$  is medium level and  $a_2$  is medium–low level. A medium level of  $a_0$  results in a starting angle of the inlet edge on the hub of  $4.5^\circ$  and when  $a_2$  is medium–low, the curve of the inlet edge changes gently as the static pressure recovery coefficient increases. Figure 9c shows that the static pressure recovery coefficient reaches the optimal value when  $a_1$  is at a medium–low level and  $a_2$  is at a medium level. A medium–low level of  $a_1$  indicates that the symmetry axis of the curve is inclined towards the shroud and a medium level of  $a_2$  indicates that the opening size and bending size of the curve are moderate. Therefore, the static pressure recovery coefficient of the diffuser will decrease if the inlet edge bends excessively or too gently. Importantly, the static pressure recovery coefficient is improved when the inlet profile is moderately bent with an axially symmetrical offset to the shroud.

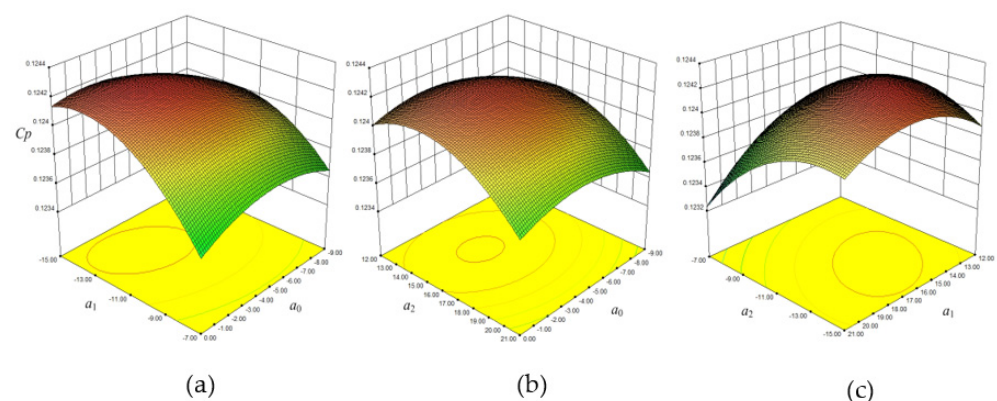


**Figure 9.** Response surface of pressure recovery coefficient in blade lean optimization (a)  $a_2 = 0$ . (b)  $a_1 = 0$ . (c)  $a_0 = 0$ .

Figure 10 shows the response surface with non-uniformity. Figure 10a shows that low levels of  $a_0$  and  $a_1$  minimize non-uniformity. When  $a_0$  is low, the starting angle of the inlet edge of the diffuser on the hub is  $9^\circ$ . When  $a_1$  is low, the axis of the curve moves from the hub side to the center of the spanwise end, the internal flow uniformity of the diffuser improves, and non-uniformity decreases. Figure 10b shows that when  $a_0$  and  $a_2$  are both at low levels, non-uniformity is lowest. When  $a_1$  is at a medium level, the contour lines of the

diffuser non-uniformity are evenly distributed, and the variation of the response surface is relatively gentle. The non-uniformity decreases with decreasing  $a_2$  but is less affected by  $a_0$ . Figure 10c shows that both  $a_2$  and  $a_1$  have the lowest non-uniformity at low levels. When the starting angle on the hub of the inlet side is large, the symmetrical axis of the inlet profile is at 1/2 of the spanwise direction and the range of starting angles for each flow surface in the spanwise direction increases. Thus, the internal flow characteristics and flow uniformity in the diffuser can be improved.

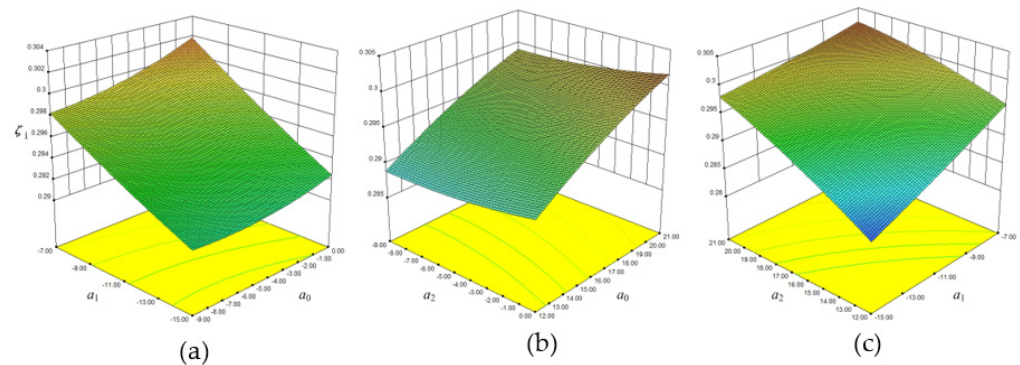


**Figure 10.** Response surface of non-uniformity in blade lean optimization. (a)  $a_2 = 0$ . (b)  $a_1 = 0$ . (c)  $a_0 = 0$ .

The factor  $a_2$  has the largest influence on the diffuser efficiency, followed by  $a_1$ , and the influence of  $a_0$  is the smallest. The diffuser efficiency increases with the increase of  $a_1$  and  $a_2$ , increasing first and then decreasing with the increase of  $a_0$ . The influence of factor  $a_1$  on the static pressure recovery coefficient of diffuser is the largest, followed by  $a_2$ , and  $a_0$  is the smallest. The static pressure recovery coefficient increases first and then decreases with the decrease of the three factors. Moreover,  $a_1$  and  $a_2$  have significant effects on the diffuser non-uniformity, while  $a_0$  has little effect on the non-uniformity. When the three factors are at a low level, the non-uniformity is the lowest, and the outlet uniformity of the diffuser is the best. The optimal blade lean scheme was obtained by considering the actual operating conditions of the multi-stage submersible pump and the effects of  $a_0$ ,  $a_1$ , and  $a_2$  on diffuser efficiency, static pressure recovery coefficient, and non-uniformity, as shown in Table 6. The results show that when  $a_0$  is at the medium level of  $-4.4$ ,  $a_1$  has the low level of  $-12$  and  $a_2$  has the medium level of  $15.16$  both the diffuser efficiency and the static pressure recovery coefficient improve.

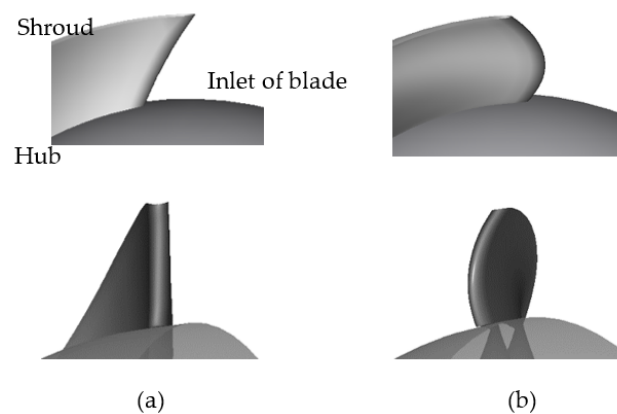
**Table 6.** Optimal solution of blade lean scheme.

	$a_0$	$a_1$	$a_2$	$\eta$ (%)	$C_p$	$\zeta_i$
Blade lean optimized diffuser	$-4.4$	$-12$	$15.16$	$95.1$	$0.1242$	$0.292$
Original diffuser	$5$	$-5$	$0$	$94.8$	$0.1210$	$0.321$

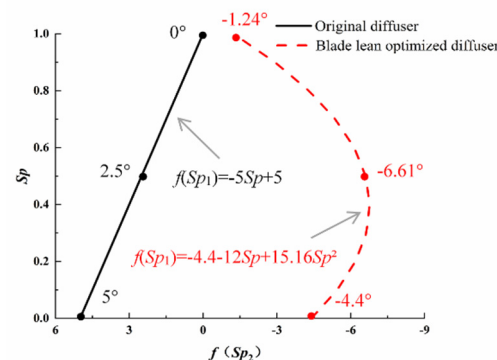
Structural changes to the inlet edge of the blade lean optimized diffuser and the original diffuser are shown in Figure 11. The inlet edge profile equation and spanwise distribution of the initial angle are illustrated in Figure 12. The starting angle of the blade lean optimized diffuser has a curved distribution, and the starting angle of the original diffuser has a linear distribution. After optimization, the governing equation of the blade inlet profile is  $f(Sp_1) = -4.4 - 12Sp + 15.16Sp^2$ , with axis  $Sp = 0.4$ . The starting angle of the hub is  $-4.4^\circ$  and the starting angle of the shroud is  $-1.24^\circ$ . The efficiency of the optimized diffuser is  $0.32\%$  higher than that of the original diffuser, and the static pressure recovery coefficient is  $2.64\%$  higher. However, the non-uniformity is  $9\%$  lower.

Figure 13 shows the static pressure and streamlines in the diffuser outlet section. Static pressure at the outlet of the blade lean optimized diffuser increases significantly, and the static pressure recovery coefficient is  $2.64\%$  higher than that of the original diffuser. This is

because the blade inlet profile of the blade lean optimized diffuser changes from a straight line to a curve, the structure of the leading edge is more in line with the fluid flow trend, making it difficult to flow off, as shown in Figure 13b. Figure 14 shows the circumferential velocity distribution along the spanwise wall at the inlet edge of the diffuser. The fluid velocity at the shroud of the blade lean optimized diffuser is significantly lower than that of the original diffuser. The blade lean scheme improves the static pressure conversion capacity of the diffuser and effectively reduces the circumferential velocity component of the fluid and velocity difference at the leading edge of the diffuser. Therefore, the local hydraulic loss of the diffuser is reduced and the diffuser efficiency and static pressure recovery coefficient are improved.



**Figure 11.** Blade inlet edge profile of diffuser in circumferential view (first row) and inlet view (second row). (a) Original diffuser. (b) Blade lean optimized diffuser.



**Figure 12.** Profiles of inlet edge and spanwise distribution of stacking angle.

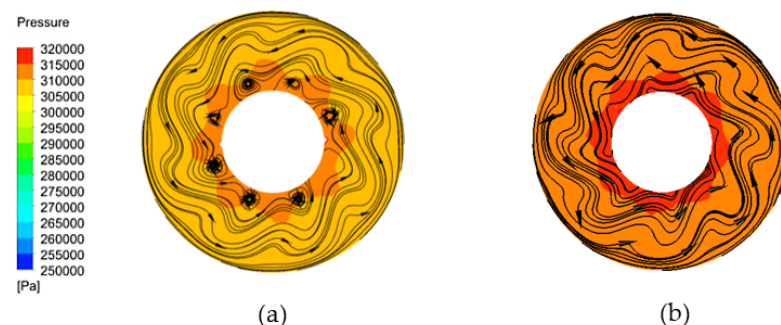


**Figure 13.** Comparison of static pressure and streamlines at diffuser outlet surface. (a) Original diffuser and (b) Blade lean optimized diffuser.

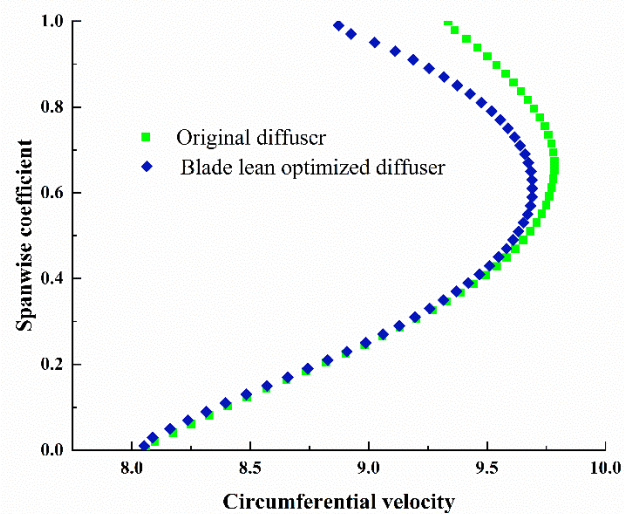


**Figure 14.** Comparison of pitch-averaged circumferential velocity distribution at leading edge of diffuser blade.

### 5.2. Response Surface of the Sweep Optimized Diffuser

As described in Section 4.2,  $b_0$  is located at the outlet edge on the hub,  $b_1$  is located at the outlet edge on the shroud, and  $b_2$  is located at the inlet edge on the hub. One factor,  $b_0$ ,  $b_1$ , or  $b_2$ , was fixed to zero and the influence of the other pair of factors on the response was analyzed. Figure 15a shows the influence of interaction between  $b_0$  and  $b_1$  on the diffuser efficiency when  $b_2$  is at a medium level. High levels of  $b_0$  and  $b_1$  resulted in the optimal diffuser efficiency. Figure 15b shows the effect of interaction between  $b_0$  and  $b_2$  on the diffuser efficiency when  $b_1$  is at a medium level. Factor  $b_2$  has a large impact on diffuser efficiency, which increases when the outlet edge on the hub moves to the outlet of the diffuser (medium–high  $b_2$ ). Figure 15c shows that the interaction between  $b_1$  and  $b_2$  has a significant influence on diffuser efficiency when  $b_0$  is at a medium level. A medium–high level of  $b_2$  and a high level of  $b_1$  resulted in the highest diffuser efficiency.

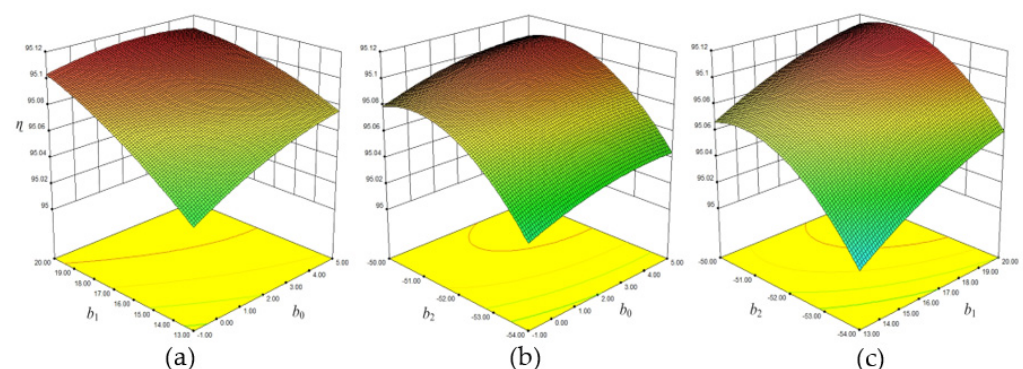


**Figure 15.** Response surface of diffuser efficiency in sweep optimization. (a)  $b_2 = 0$ . (b)  $b_1 = 0$ . (c)  $b_0 = 0$ .

Figure 16a shows that the static pressure recovery coefficient reaches the highest value when  $b_0$  is low and  $b_1$  is high. When the blade outlet on the hub moves towards the inlet of the diffuser (low  $b_0$ ) and the blade outlet on the shroud side moves towards the outlet of the diffuser (high  $b_1$ ), the static pressure recovery capacity of the diffuser improved. Figure 16b shows that the static pressure recovery coefficient is optimal when  $b_0$  is low and  $b_2$  is medium. Figure 16c shows that the static pressure recovery coefficient reaches the highest value when  $b_1$  is high and  $b_2$  is medium. The blade outlet edge on the hub moves towards the inlet of the diffuser (low  $b_0$ ) and the blade outlet edge on the shroud moves

towards the outlet of diffuser (high  $b_1$ ), whereas the position of the blade inlet edge does not change at medium  $b_2$  and the static pressure recovery coefficient can be increased.

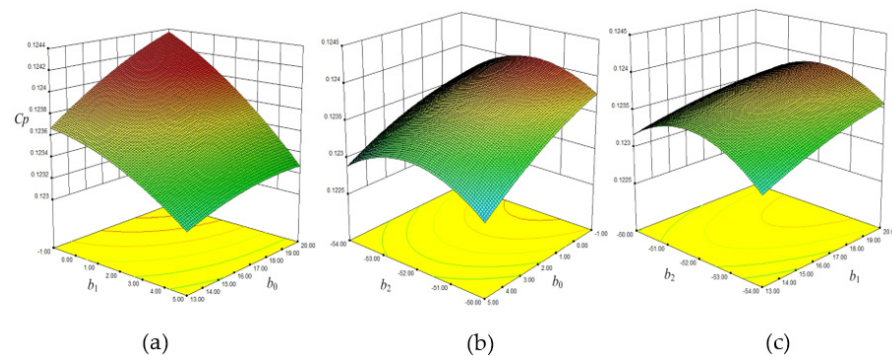


**Figure 16.** Response surface of pressure recovery coefficient in sweep optimization. (a)  $b_2 = 0$ . (b)  $b_1 = 0$ . (c)  $b_0 = 0$ .

Figure 17a shows that non-uniformity decreases when high  $b_0$  interacts with high  $b_1$ . The outlet edge of the diffuser moves from the shroud to the hub (high  $b_0$  and  $b_1$ ), which can improve the flow uniformity in the diffuser. Figure 17b shows that non-uniformity is relatively low when  $b_0$  is high. Factor  $b_2$  has no obvious effect on non-uniformity and provided  $b_0$  moves to a higher level, flow non-uniformity in the diffuser will decrease. A high level of  $b_0$  is the key to optimizing flow uniformity in the diffuser but does not improve the static pressure recovery coefficient. Figure 17c shows that flow non-uniformity in the diffuser is low when  $b_1$  is high. The change in direction of flow on the inlet side of the diffuser hub has very little effect on non-uniformity in the diffuser, while moving the outlet side of the diffuser towards the outlet direction (high  $b_0$  and  $b_1$ ) improves the flow uniformity.

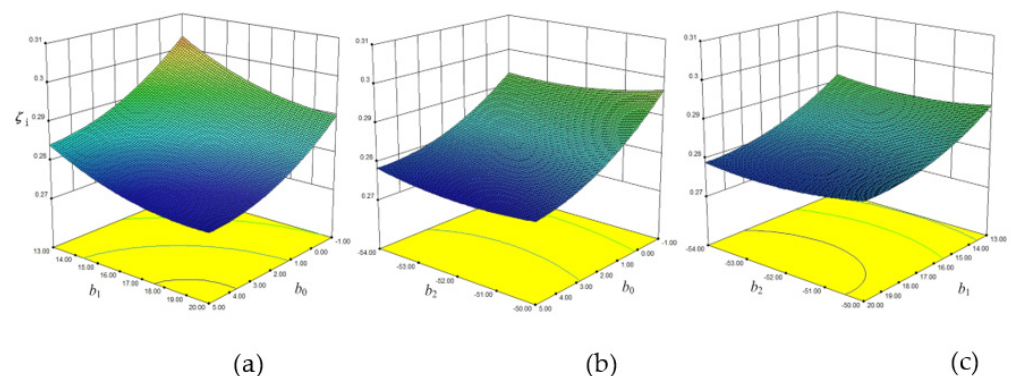


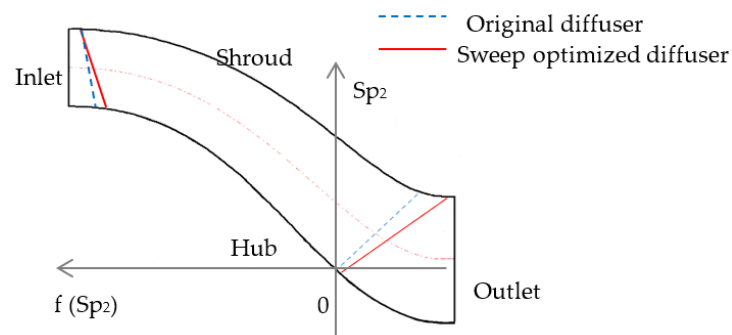
**Figure 17.** Response surface of non-uniform in sweep optimization. (a)  $b_2 = 0$ . (b)  $b_1 = 0$ . (c)  $b_0 = 0$ .

According to the measured data and response surface analysis, the factor  $b_2$  has the largest influence on the diffuser efficiency, followed by  $b_1$ , and the influence of  $b_0$  is the smallest. The diffuser efficiency exhibits an upward trend with increasing  $b_1$  and  $b_0$  and an inverted-U trend with increasing  $b_2$ . The influence of factor  $b_0$  on the static pressure recovery coefficient of diffuser is the largest, followed by  $b_2$ , and  $b_1$  is the smallest. The static pressure recovery coefficient increases with decreasing  $b_0$ , increases slowly with increasing  $b_1$ , and first increases and then decreases with increasing  $b_2$ . At the same time, non-uniformity decreases with increasing  $b_0$  and  $b_1$ , whereas changes in  $b_2$  have very little effect on flow uniformity. The optimal solution was obtained by considering the influence of  $b_0$ ,  $b_1$ , and  $b_2$  on diffuser efficiency, static pressure recovery coefficient, and non-uniformity, as shown in Table 7. The results show that when  $b_0$  has the medium–low level of 1.5,  $b_1$  has the high level of 20, and  $b_2$  has the medium level of  $-52$ , the diffuser efficiency and static pressure recovery coefficient can be improved.

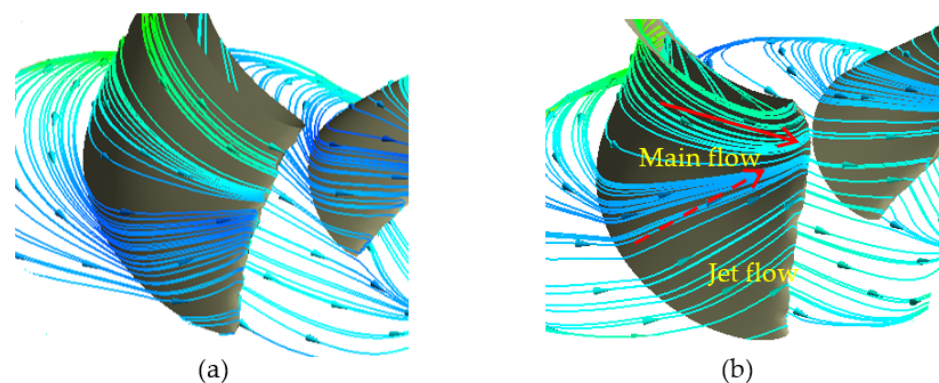
**Table 7.** Optimal solution of sweep scheme.

	$b_0$	$b_1$	$b_2$	$\eta$ (%)	$C_p$	$\zeta_i$
Sweep optimized diffuser	1.5	20	−52	95.21	0.1245	0.279
Original diffuser	0	14	−52.4	94.8	0.1210	0.321

Figure 18 shows the inlet and outlet profile positions of the original diffuser and the sweep optimized diffuser on the meridional plane. In the original pump,  $b_0 = 0$ ,  $b_1 = 14$ , and  $b_2 = -52.4$ . In the sweep scheme, the values are  $b_0 = 1.5$ ,  $b_1 = 20$ , and  $b_2 = -52$ . The position of the shroud surface at the blade outlet ( $b_1$ ) changes greatly. When the shroud edge of the blade outlet moves towards the outlet of the diffuser, the influence of  $b_1$  on the diffuser can be clearly observed.

**Figure 18.** Comparison of sweep optimized meridional plane and the original of diffuser.

The optimized blade trailing edge extends the diffuser outlet on the shroud side, as shown in Figure 18. The increased blade trailing edge can better drain the fluid to the diffuser outlet, whereas there is sufficient time for velocity exchange with the high-speed main body when the fluid flows through the extended blade trailing edge (Figure 19b), thereby reducing the velocity gradient and improving flow uniformity at the outlet of the diffuser. In Figure 19a, low-energy fluid in the original diffuser does not fully mix with the high-speed mainstream and large differences in velocity lead to increased hydraulic losses in the diffuser, which affects the outlet flow uniformity. Therefore, the flow inside the sweep optimized diffuser is more reasonable. Compared with the original diffuser, flow non-uniformity is reduced by 13.1%.

**Figure 19.** Comparison of the streamlines of blade outlet edge. (a) Original diffuser. (b) Sweep optimized diffuser.

## 6. Discussion

The origin of the hub corner separation vortex can be explained by reference to Figure 20. The vortex originates from two positions: the inlet of the diffuser, represented by

A, and the central of the diffuser, represented by B. In region A1, the curvature difference between the meridian shroud and the hub surface leads to the development of spanwise differential pressure, driving secondary flow from the shroud to the hub, which scours the inlet edge, thus forming a spanwise pressure difference, represented by region L. As the flow develops, swirling flow occurs at the hub in region A2 and rushes against the transverse pressure gradient towards the PS. In the center of the diffuser (region B1), the working fluid must flow against the reverse pressure gradient, resulting in an increase in low-momentum fluid on the hub. Then, the increased amount of low-momentum fluid is deflected towards the SS under the transverse differential pressure at the hub in region B2. Finally, a large hub corner separation vortex appears in the corner of the blade, accounting for about 1/3 of the area of the hub. In a previous study [20], the spanwise secondary flow from shroud to hub at the trailing edge of the diffuser was shown to scour low-energy fluid, thereby inhibiting the hub corner vortex. However, our results suggest that low-energy fluid accumulated on the suction surface cannot overcome the spanwise pressure difference between the shroud and the hub and can only reverse the flow along the hub surface, forming a secondary flow angle to suppress the vortex in region B3.

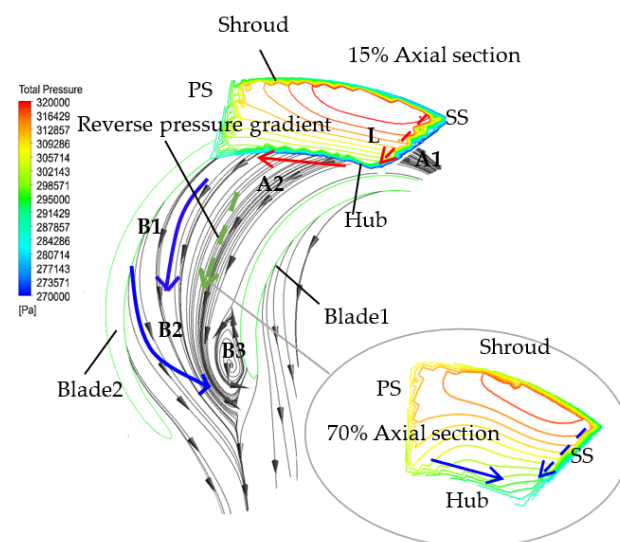


**Figure 20.** Onset of hub corner separation depicted by limiting streamlines and total pressure.

To explain the improvement in diffuser efficiency and diffuser uniformity, the spanwise/transverse pressure difference in the diffuser were quantified, as shown in Figures 21 and 22. At the inlet of the diffuser, the spanwise pressure difference in the blade lean optimized diffuser is significantly higher, resulting in enhanced transverse secondary flow (Figure 21). The spanwise pressure difference in the sweep optimized diffuser is significantly lower than in the blade lean optimized diffuser; therefore, the transverse pressure difference caused by spanwise secondary flow at the inlet of the diffuser is weakened. Moreover, both the transverse pressure differences at the inlet of the sweep optimized diffuser and blade lean optimized diffuser increase (Figure 22), which offsets the transverse pressure difference and suppresses the hub corner separation vortex.

At the outlet of the diffuser, the spanwise pressure difference at the trailing edge in the blade lean optimized diffuser is lower than in the original diffuser, as shown in Figure 19, which is not conducive to improving the diffuser performance. However, the spanwise pressure difference at the trailing edge in the sweep optimized diffuser is highest; therefore, low-energy fluid in the corner area becomes caught up in the main flow and is dragged toward the outlet of the diffuser, thus improving flow uniformity in the diffuser. When the low-energy fluid at the trailing edge of the diffuser is restrained and the difference between the mainstream velocity is weakened, mixing losses at the diffuser outlet are reduced and the hydraulic efficiency of the diffuser is improved.

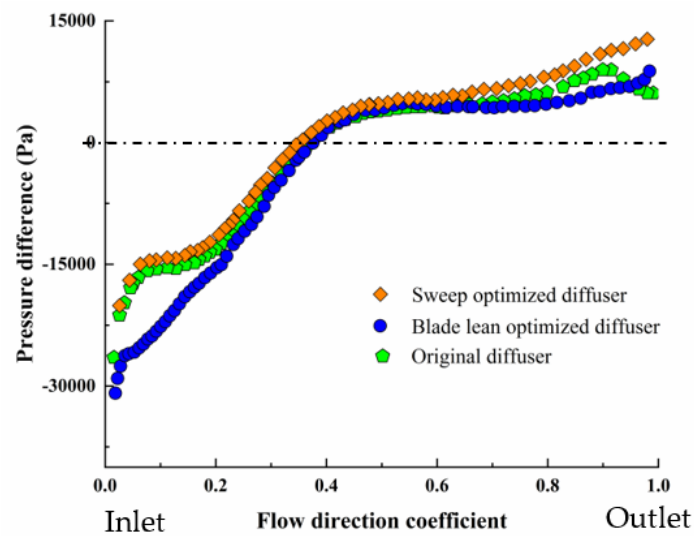


Figure 21. Comparison of spanwise pressure difference from hub to shroud of suction surface.

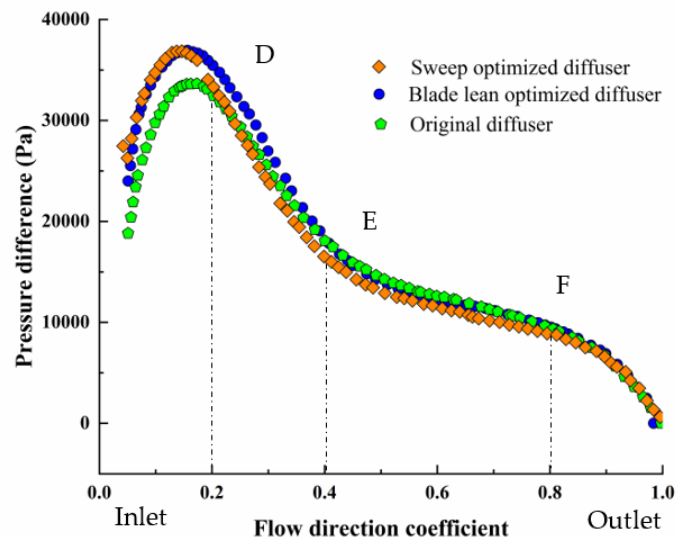


Figure 22. Comparison of transverse pressure difference from PS to SS on hub surface.

The reduced low-energy fluid in the center of the diffuser and the spanwise differential pressure drainage at the trailing edge of the diffuser lead to more uniform outflow. In Figure 21, the spanwise pressure difference in the center of the diffuser changes from negative to positive, and the direction is reversed. Therefore, the low-energy fluid originally returns from the hub to the low-pressure area in the center, which suppresses the corner separation vortex and improves the outlet flow uniformity in the diffuser. In Figure 22, the transverse pressure difference in the sweep optimized diffuser is less than in the blade lean optimized diffuser in the DF stage; however, the reverse pressure gradient in the DE stage is greater than in the blade lean optimized diffuser. The amount of low-energy fluid in the center of the diffuser increases and the reduced transverse pressure difference in the center cannot reduce the amount of low-energy fluid in the suction surface corner. However, the transverse pressure difference between the PS and SS in the EF stage decreases; therefore, the reverse pressure gradient in the flow direction decreases and the amount of low-energy fluid in the corner decreases.

Figure 23 compares the static pressure on the shroud of the diffuser under different scenarios. The static pressure on the shroud of the blade lean optimized diffuser is higher than that of the original diffuser, and the increase in static pressure on the PS is more obvious. Therefore, the blade lean optimized diffuser can convert more kinetic energy

in the fluid into static pressure energy and the static pressure recovery coefficient of the diffuser can be improved. The static pressure on the shroud of the sweep optimized diffuser does not always increase; however, it is higher than those of other diffusers at the stage of 10–65% flow direction and decreases at the outlet section. The reason for this is that the flow direction at the outlet of the sweep optimized diffuser changes greatly and the distance between the working fluid flowing through the diffuser and the trailing edge of the blade increases. Thus, the static pressure decreases and the static pressure recovery coefficient of the diffuser does not increase significantly.

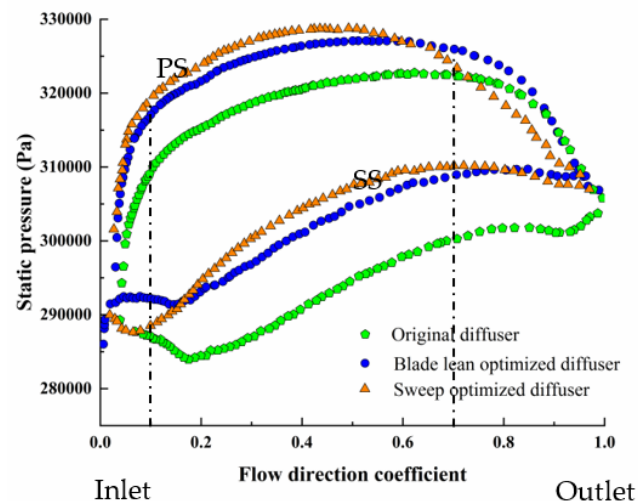


Figure 23. Static pressure comparison around shroud surface of diffuser.

## 7. Conclusions

Aimed at controlling the hub corner separation vortex and corresponding high hydraulic losses in the bowl diffuser of a multistage submersible pump, the diffuser was optimized in terms of blade lean and sweep. The blade structure can be controlled digitally and accurately using parametric equations. CFD simulations and central combination tests were used to optimize different blade lean and sweep schemes. The internal flow field and static pressure distribution in the diffuser were thoroughly investigated.

At the hub corner of the diffuser, the low-energy fluid induced by spanwise and transverse pressure at the inlet of the diffuser blade overcomes the streamwise pressure gradient and accumulates in the mid-section of the suction surface. However, the accumulated low-energy fluid cannot overcome the spanwise pressure difference between the shroud and the hub, the flow direction is reversed toward the inlet, and the hub corner vortex forms. Optimization of the blade lean and sweep can improve the transverse pressure in the diffuser. In particular, the hub–shroud spanwise pressure can be enhanced in order to drive the low-energy fluid towards the center of the blade, rather than reversing it. This suppresses the hub corner vortex and improves the hydraulic performance of the diffuser.

In the blade lean scheme, the transverse pressure difference at the inlet of the diffuser increases, which inhibits the formation of the hub corner separation vortex. However, the spanwise pressure difference at the inlet of the suction surface increases, and the spanwise pressure difference at the trailing edge decreases, which does not improve the performance of the diffuser. Moreover, since the structure of the leading edge of the blade changes and the fluid flows close to the blade after entering the diffuser, flow separation is difficult to induce. The fluid kinetic energy and static pressure energy are fully converted, the static pressure recovery coefficient increases by 2.64% compared with the original diffuser, and the diffuser efficiency increases by 0.32%. Optimization of blade lean can improve the static pressure recovery coefficient and diffuser efficiency but does not improve flow uniformity in the diffuser.

The sweep scheme can reduce the spanwise pressure difference and transverse pressure difference at the inlet of the diffuser, increase the spanwise pressure difference at the outlet of the diffuser, inhibit the formation of the hub corner separation vortex, and improve the flow uniformity of the diffuser. However, the increase in the reverse pressure gradient in the flow direction of the diffuser limits the improvement in diffuser efficiency. Sweep design can effectively reduce flow non-uniformity in the diffuser; however, the influence of the static pressure recovery coefficient is small.

**Author Contributions:** Conceptualization, P.C. and C.N.; Formal analysis, C.N. and X.G.; Methodology, C.N. and R.Z.; Project administration, P.C.; Software, R.Z.; Writing—original draft, C.N.; Writing—review & editing, X.G. All authors have read and agreed to the published version of the manuscript.

**Funding:** This research was funded by the Natural Science Foundation of Jiangsu Province: BK20190847, China Postdoctoral Science Foundation: 2019M661744, the National Natural Science Foundation of China: 51879120, and the Priority Academic Program Development of Jiangsu Higher Education Institutions (PAPD).

**Institutional Review Board Statement:** Not applicable.

**Informed Consent Statement:** Not applicable.

**Data Availability Statement:** The data that support the findings of this study are available from the corresponding author upon reasonable request.

**Acknowledgments:** A huge thanks is due to the editor and reviewers for their valuable comments to improve the quality of this paper.

**Conflicts of Interest:** The authors declare no conflict of interest.

## Abbreviations

$C_p$	Static pressure recovery coefficient
CCD	Center composite design
$H$	Head (m)
PS	Pressure surface of blade
SS	Suction surface of blade
$k$	Turbulent kinetic energy ( $\text{m}^2/\text{s}^2$ )
$P_{\text{in}}$	Total pressure of pump inlet (Pa)
$P_{\text{out}}$	Total pressure of pump outlet (Pa)
$P_{\text{t3}}$	Total pressure of diffuser inlet (Pa)
$P_{\text{t4}}$	Total pressure of diffuser outlet (Pa)
$P_{\text{s3}}$	Static pressure of diffuser inlet (Pa)
$P_{\text{s4}}$	Static pressure of diffuser outlet (Pa)
$\rho$	Density of fluid ( $\text{kg}/\text{m}^3$ )
$\mu_t$	Turbulent viscosity ( $\text{kg}/\text{m}\cdot\text{s}$ )
$\varepsilon$	Turbulent energy dissipation ( $\text{m}^2/\text{s}^3$ )
$\phi_{\text{Hub}}$	Wrap angle of hub ( $^\circ$ )
$\phi_{\text{Shroud}}$	Wrap angle of shroud ( $^\circ$ )
$\theta$	Starting angle ( $^\circ$ )
$\Delta\theta$	Starting angle difference ( $^\circ$ )
$\theta_{\text{Hub}}$	Starting angle of hub flow surface ( $^\circ$ )
$\theta_{\text{Shroud}}$	Starting angle of shroud flow surface ( $^\circ$ )
$\beta$	Sweep angle of diffuser ( $^\circ$ )
$\eta$	Efficiency of diffuser (%)
$\zeta_i$	Non-uniformity

## References

1. Wang, H.L.; Hu, Q.X.; Yang, Y.; Wang, C. Performance Differences of Electrical Submersible Pump under Variable Speed Schemes. *Int. J. Simul. Model.* **2021**, *20*, 76–86. [[CrossRef](#)]
2. Zhou, J.; Zhao, M.; Wang, C.; Gao, Z. Optimal Design of Diversion Piers of Lateral Intake Pumping Station Based on Orthogonal Test. *Shock. Vib.* **2021**, *2021*, 6616456. [[CrossRef](#)]
3. Shi, L.; Zhu, J.; Tang, F.; Wang, C. Multi-Disciplinary Optimization Design of Axial-Flow Pump Impellers Based on the Approximation Model. *Energies* **2020**, *13*, 779. [[CrossRef](#)]
4. Zhang, L.; Wang, C.; Zhang, Y.; Xiang, W.; He, Z.; Shi, W. Numerical study of coupled flow in blocking pulsed jet impinging on a rotating wall. *J. Braz. Soc. Mech. Sci. Eng.* **2021**, *43*, 508. [[CrossRef](#)]
5. Wang, H.; Long, B.; Wang, C.; Han, C.; Li, L. Effects of the Impeller Blade with a Slot Structure on the Centrifugal Pump Performance. *Energies* **2020**, *13*, 1628. [[CrossRef](#)]
6. Wang, H.; Qian, Z.; Zhang, D.; Wang, T.; Wang, C. Numerical Study of the Normal Impinging Water Jet at Different Impinging Height, Based on Wray–Agarwal Turbulence Model. *Energies* **2020**, *13*, 1744. [[CrossRef](#)]
7. Bellary, S.A.I.; Husain, A.; Samad, A. Effectiveness of meta-models for multi-objective optimization of centrifugal impeller. *J. Mech. Sci. Technol.* **2014**, *28*, 4947–4957. [[CrossRef](#)]
8. Bellary, S.A.I.; Samad, A.; Couckuyt, I.; Dhaene, T. A comparative study of kriging variants for the optimization of a turbomachinery system. *Eng. Comput.* **2016**, *32*, 49–59. [[CrossRef](#)]
9. Huang, K.L.; Yuan, J.P.; Si, Q.R.; Lin, G. Numerical simulation of pressure pulsation in multistage centrifugal pump under multi-operation condition. *J. Drain. Irrig. Mach. Eng.* **2019**, *37*, 387–392.
10. Tong, S.G.; Zhao, H.; Liu, H.Q.; Tong, Z.M.; Yue, Y.U.; Tang, N. Optimization calculation method for efficiency of multistage split case centrifugal pump. *J. Zhejiang Univ. Eng. Sci.* **2019**, *53*, 988–996.
11. Stel, H.; Sirino, T.; Ponce, F.; Chiva, S.; Morales, R. Numerical investigation of the flow in a multistage electric submersible pump. *J. Pet. Sci. Eng.* **2015**, *136*, 41–54. [[CrossRef](#)]
12. Heo, M.W.; Ma, S.-B.; Shim, H.S.; Kim, K.Y. High-efficiency design optimization of a centrifugal pump. *J. Mech. Sci. Technol.* **2016**, *30*, 3917–3927. [[CrossRef](#)]
13. Murugesan, C.; Rudramoorthy, R. Numerical And Experimental Study Of Single stage And Multistage Centrifugal Mixed Flow Submersible Borewell Pumps. *Int. J. Fluid Mach. Syst.* **2016**, *9*, 107–118. [[CrossRef](#)]
14. Kim, J.-H.; Cho, B.-M.; Kim, S.; Lee, Y.-K.; Choi, Y.-S. Steady and Unsteady Flow Characteristics of a Multi-stage Centrifugal Pump under Design and Off-design Conditions. *Int. J. Fluid Mach. Syst.* **2019**, *12*, 64–70. [[CrossRef](#)]
15. Rosic, B.; Xu, L. Blade Lean and Shroud Leakage Flows in Low Aspect Ratio Turbines. *J. Turbomach.* **2011**, *134*, 031003. [[CrossRef](#)]
16. Razavi, S.R.; Sammak, S.; Boroomand, M. Multidisciplinary Design and Optimizations of Swept and Leaned Transonic Rotor. *J. Eng. Gas Turbines Power* **2017**, *139*, 122601. [[CrossRef](#)]
17. He, X.; Zheng, X. Mechanisms of Sweep on the Performance of Transonic Centrifugal Compressor Impellers. *Appl. Sci.* **2017**, *7*, 1081. [[CrossRef](#)]
18. He, X.; Zheng, X. Performance improvement of transonic centrifugal compressors by optimization of complex three-dimensional features. *Proc. Inst. Mech. Eng. Part G J. Aerosp. Eng.* **2016**, *231*, 2723–2738. [[CrossRef](#)]
19. Bagshaw, D.A.; Ingram, G.; Gregory-Smith, D.G.; Stokes, M.R.; Harvey, N.W. The design of three-dimensional turbine blades combined with profiled endwalls. *Proc. Inst. Mech. Eng. Part A J. Power Energy* **2008**, *222*, 93–102. [[CrossRef](#)]
20. Goto, A.; Zangeneh, M. Hydrodynamic Design of Pump Diffuser Using Inverse Design Method and CFD. *J. Fluids Eng.* **2002**, *124*, 319–328. [[CrossRef](#)]
21. Goto, A.; Nohmi, M.; Sakurai, T.; Sogawa, Y. Hydrodynamic Design System for Pumps Based on 3-D CAD, CFD, and Inverse Design Method. *J. Fluids Eng.* **2002**, *124*, 329–335. [[CrossRef](#)]
22. Scillitoe, A.; Tucker, P.G.; Adami, P. Numerical Investigation of Three-Dimensional Separation in an Axial Flow Compressor: The Influence of Freestream Turbulence Intensity and Endwall Boundary Layer State. *J. Turbomach.* **2016**, *139*, 021011. [[CrossRef](#)]
23. Şahin, F.C. Experimental investigation on flow improvement in compressor cascades. *Int. J. Energy Res.* **2016**, *41*, 526–539. [[CrossRef](#)]
24. Ananthkrishnan, K.; Govardhan, M. Influence of fillet shapes on secondary flow field in a transonic axial flow turbine stage. *Aerosp. Sci. Technol.* **2018**, *82–83*, 425–437. [[CrossRef](#)]
25. Shi, W.; Zhou, L.; Lu, W.; Xu, L.; Li, W. Numerical Simulation and Experimental Study of Different Stages Deep-Well Centrifugal Pump. *J. Comput. Theor. Nanosci.* **2013**, *10*, 2897–2901. [[CrossRef](#)]
26. Zhou, L.; Shi, W.; Li, W.; Agarwal, R. Numerical and Experimental Study of Axial Force and Hydraulic Performance in a Deep-Well Centrifugal Pump With Different Impeller Rear Shroud Radius. *J. Fluids Eng.* **2013**, *135*, 104501. [[CrossRef](#)]
27. Yuan, S.Q.; He, W.T.; Si, Q.R.; Yuan, J.P.; Zhang, H.Y.; Cui, Q.L. Numerical simulation on gas-liquid two-phase flow in centrifugal pump based on MUSIG model. *J. Drain. Irrig. Mach. Eng.* **2021**, *39*, 1–7.
28. Yakhot, V.; Orszag, S.A. Renormalization group analysis of turbulence. I. Basic theory. *J. Sci. Comput.* **1986**, *1*, 3–51. [[CrossRef](#)]
29. Lam, S.H. On the RNG theory of turbulence. *Phys. Fluids A Fluid Dyn.* **1992**, *4*, 1007–1017. [[CrossRef](#)]
30. Mompean, G. Numerical simulation of a turbulent flow near a right-angled corner using the Speziale non-linear model with RNG  $K-\epsilon$  equations. *Comput. Fluids* **1998**, *27*, 847–859. [[CrossRef](#)]

- 
31. Cao, P.; Zhu, R.; Yin, G. Spike-type disturbances due to inlet distortion in a centrifugal pump. *Renew. Energy* **2021**, *165*, 288–300. [[CrossRef](#)]
  32. Zhou, L.; Wang, W.; Hang, J.; Shi, W.; Yan, H.; Zhu, Y. Numerical Investigation of a High-Speed Electrical Submersible Pump with Different End Clearances. *Water* **2020**, *12*, 1116. [[CrossRef](#)]
  33. Zhou, L.; Bai, L.; Shi, W.; Li, W.; Wang, C.; Ye, D. Numerical analysis and performance experiment of electric submersible pump with different diffuser vanes number. *J. Braz. Soc. Mech. Sci. Eng.* **2018**, *40*, 89. [[CrossRef](#)]